

Hierarchical NMPC for obstacle avoidance on skid-steer loaders[★]

Ruairi Moran^{*} Sheila Bagley^{**} David Pasley^{**}
Seth Kasmann^{**} Rob Martin^{**} Scott Pfursich^{**}
Shane Trimble^{**} James Dianics^{**} Pantelis Sopasakis^{*}

^{*} Queen's University Belfast, EEECS, i-AMS Centre, Ashby Building,
BT9 5AH, Belfast UK (email: rmoran05@qub.ac.uk)

^{**} EquipmentShare, 5710 Bull Run Dr, Columbia, MO 65201, USA.

Abstract: This paper introduces a novel NMPC formulation for real-time obstacle avoidance on heavy equipment by modeling both vehicle and obstacles as convex superellipsoids. The combination of this approach with the separating hyperplane theorem and Optimization Engine (OpEn) allows to achieve efficient obstacle avoidance in autonomous heavy equipment and robotics. We demonstrate the efficacy of the approach through simulated and experimental results, showcasing a skid-steer loader's capability navigate in obstructed environments.

Keywords: Obstacle avoidance, Nonlinear MPC

1. INTRODUCTION

In the rapidly evolving domains of robotics and autonomous systems, two critical motion challenges stand out: path planning and trajectory planning (Khan et al., 2021). Path planning involves finding a global path through complex environments that a mobile robot can follow. Trajectory planning involves finding a local path between points of the global path, while avoiding unexpected obstacles. This paper explores trajectory planning. Achieving safe and efficient obstacle avoidance is a challenge that spans various engineering applications, from autonomous ground vehicles (AGVs) (Liu et al., 2018) and drones (Xue and Gonsalves, 2021) to industrial robots (Gai et al., 2019) and many more (Patle et al., 2019). This work is applied to skid-steer heavy equipment in a construction site environment (Crane III et al., 1995; Melenbrink et al., 2020), where ensuring operator safety is paramount (Teizer et al., 2010). Skid-steer vehicles have many applications due to their simple mechanical structure and high mobility (Khan et al., 2021).

To address this challenge, we explore the optimization-based approach of a nonlinear model predictive controller (NMPC) (Grüne et al., 2017). An NMPC calculates safe and feasible trajectories and control inputs for a vehicle in real time, through a combination of nonlinear model-based prediction and constrained optimization. This paper proposes a collision avoidance condition for an NMPC, derived from the combination of the separating hyperplane theorem (SHT) (Boyd and Vandenberghe, 2004, Sec. 2.5.1) and superellipsoids.

Superellipsoids, a generalization of ellipsoids and rectangles, offer versatile object representation. Superellipsoids have been used to represent objects for obstacle avoidance (Menon et al., 2017; Smith et al., 2017), and the work

[★] This work has been supported by the research project “BotDozer,” which is funded by EPSRC and EquipmentShare.

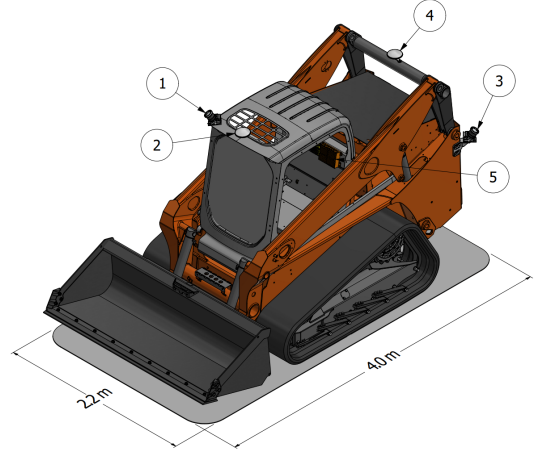


Fig. 1. EquipmentShare's compact track loader, *Moe*. The labels are: 1. front LiDAR, 2. front GNSS, 3. rear LiDAR, 4. rear GNSS, 5. IMU and TX2.

in (Pauls et al., 2022) recently recommended superellipsoid representation for motion planning.

In this paper we implement a navigation system as a two-layer hierarchical NMPC (Scattolini, 2009), with a high-level NMPC layer that involves the proposed collision avoidance condition, and a low-level NMPC layer that tracks the reference trajectory from the high-level layer. Hierarchical NMPC enables different sampling times and control horizons for each layer, ensuring quick and adaptive responses to environmental changes at the low layer while allowing optimal trajectory planning at the high layer.

Note that generally mobile robot path planning and obstacle avoidance techniques model the vehicle as a point or an ellipsoid, and obstacles as ellipsoids or polygons Khan (2022); Rafai et al. (2022). Such approaches can naturally lead to overly conservative overapproximation, thus neces-

situating a large vehicle-to-obstacle distance. We contribute an approach that models every object as a superellipsoid. Additionally, we cast the NMPC problem in a form that allows its fast solution using OpEn and demonstrate the trajectory-planning capability with a real-time application.

Notation. Let $\mathbb{N}_{[t_1, t_2]}$ denote the set of natural numbers from t_1 to t_2 , \mathbb{R} the set of real numbers, and \mathbb{R}^n the n -dimensional real space equipped with the standard inner product $\langle \cdot, \cdot \rangle$. Then, the support function of a set $\mathcal{X} \subseteq \mathbb{R}^n$ at $x \in \mathbb{R}^n$ is defined by $\delta_{\mathcal{X}}^*(x) = \sup_{y \in \mathcal{X}} \langle x, y \rangle$, and the p -norm of x is defined by $\|x\|_p = (\sum_{i=1}^n |x_i|^p)^{\frac{1}{p}}$, where $p \in [1, \infty)$. We denote the unit p -norm ball $\mathcal{B}_p = \{x \in \mathbb{R}^n : \|x\|_p \leq 1\}$. Lastly, we define the matrix-set product $A\mathcal{X} = \{Ax, \forall x \in \mathcal{X}\}$.

2. VEHICLE

The vehicle in this paper is the compact track loader (CTL) *Moe*, illustrated in Fig. 1, which is a type of skid-steer that moves on two parallel tracks. The arm and bucket are held in place in this work.

The global frame of reference is the North-East-Down (NED) coordinate system (Cai et al., 2011, Sec. 2.2). We denote a position on the North axis by x_1 and on the East axis by x_2 . The body-fixed frame of reference uses the same coordinate system fixed to the vehicle's principal axes. The vehicle's heading is denoted θ , where $\theta = 0$ corresponds to the vehicle facing North. A positive heading corresponds to a clockwise rotation of the vehicle with respect to the global frame of reference.

A CTL steers by rotating the tracks at different rates. The dynamics is nonholonomic. The vehicle's state $z = (c, \theta, v)$ consists of the position $c \in \mathbb{R}^2$, heading $\theta \in (-\pi, \pi]$, and orbital velocity $v \in \mathbb{R}$. The vehicle's input $u = (r, s)$ consists of the throttle $r \in [-1, 1]$ and spin $s \in [-1, 1]$. We use the unicycle model, which is a simplified differential drive (LaValle, 2006, Sec. 15.4.1)

$$\dot{c}_1 = v \cos(\theta), \quad (1a)$$

$$\dot{c}_2 = v \sin(\theta), \quad (1b)$$

$$\dot{\theta} = \alpha s, \quad (1c)$$

$$\dot{v} = \beta (rv_{\max} - v), \quad (1d)$$

where $\alpha, \beta, v_{\max} \geq 0$ are tuning parameters for adapting the model to different terrains (softer ground will result in smaller α and β) and different vehicles (v_{\max} is the maximum velocity). Despite its simplicity, the model is sufficient for trajectory planning and control tasks.

The CTL uses a diesel-hydraulic powertrain to drive both tracks separately. The sensors on board include an iNEMO ISM330DLC IMU updating at 208Hz, two Swift Navigation Piksi Multi GNSS units at 10Hz, and two LiDAR units at 20Hz. These provide readings with standard measurement error of the vehicle's latitude and longitude to 10mm, altitude to 15mm, heading to 0.6° , and obstacle detection within a 35m radius.

The sensors are connected via local Ethernet to an NVIDIA Jetson TX2, which is the main computational unit on the vehicle. The TX2 is connected to the vehicle control unit (VCU) over controller area network (CAN)

bus, which allows the TX2 to override the original equipment manufacturer's (OEM) throttle and spin inputs. The on-board equipment is depicted in Fig. 1.

The TX2 codebase is primarily written in Python. The vehicle state and control inputs are logged at 10Hz. The controllers in Section 4 is built with Optimization Engine (OpEn) (Sopasakis et al., 2020), an open-source code generation software for embedded nonlinear optimization that runs in Rust. OpEn was chosen because it has low memory requirements, involves simple algorithm operations, the generated Rust code is provably memory safe, and has been shown to be faster than interior point and sequential quadratic programming implementations (Sathya et al., 2018).

3. COLLISION AVOIDANCE FORMULATION

3.1 Introducing superellipsoids

We will be modeling the vehicle and obstacles by sets of the form

$$\mathcal{X} = \{RSx + c \mid x \in \mathcal{B}_p\}, \quad (2)$$

where $x \in \mathbb{R}^2$, $p \in [2, \infty)$, $S \in \mathbb{R}^{2 \times 2}$ is a diagonal scaling matrix, $S = \text{diag}(s_1, s_2)$, where $s_1, s_2 > 0$, $R_\theta \in \text{SO}(2)$ is the elementary rotation matrix

$$R_\theta = \begin{bmatrix} \cos \theta & -\sin \theta \\ \sin \theta & \cos \theta \end{bmatrix}, \quad (3)$$

where $\theta \in (-\pi, \pi]$ and $c \in \mathbb{R}^2$ is the center point. We restrict $p \geq 2$ where the sets are smooth and convex. When $p = 2$, Equation (2) describes an ellipsoid. The matrix product RS scales the set \mathcal{B}_p by s_1 on the North axis, by s_2 on the East axis, and rotates the scaled set clockwise about the center point through the angle θ . Note that R is orthogonal and RS is nonsingular.

Superellipsoid is the umbrella term for a set described by Equation (2) (Weisstein, 2002, p.1760). The set is also called a Lamé curve (Gridgeman, 1970). In this paper we use superellipsoids with $p = 3$ (see Fig. 2). Higher values of p will make the shape look closer to a rectangle.

3.2 Collision detection

Let us denote the vehicle set \mathcal{V} and an obstacle set \mathcal{E} . Hereafter, we will only consider one obstacle, however, the extension to multiple obstacles will be obvious.

A collision between two sets can be detected by a condition that checks if the sets are disjoint. We know from the separating hyperplane theorem (Boyd and Vandenberghe, 2004, Sec. 2.5.1) that if two convex sets \mathcal{V} and \mathcal{E} are disjoint, there exists a separating hyperplane such that \mathcal{V} is on one side and \mathcal{E} is on the other. There are several converse SHTs, such as the separating axis theorem (SAT) (Ericson, 2004, Sec. 5.2.1). We propose Theorem 1.

Theorem 1. (Converse SHT). Let $\mathcal{V}, \mathcal{E} \subseteq \mathbb{R}^n$ be nonempty sets, there exists $a \in \mathbb{R}^n$, and

$$\sup_{x \in \mathcal{V}} \langle a, x \rangle < \inf_{x \in \mathcal{E}} \langle a, x \rangle. \quad (4)$$

Then \mathcal{V} and \mathcal{E} are disjoint, i.e., $\mathcal{V} \cap \mathcal{E} = \emptyset$.

Proof. Suppose Equation (4) holds, but \mathcal{V} and \mathcal{E} are not disjoint, i.e., $\mathcal{V} \cap \mathcal{E} \neq \emptyset$. Take $y \in \mathcal{V} \cap \mathcal{E}$. Then

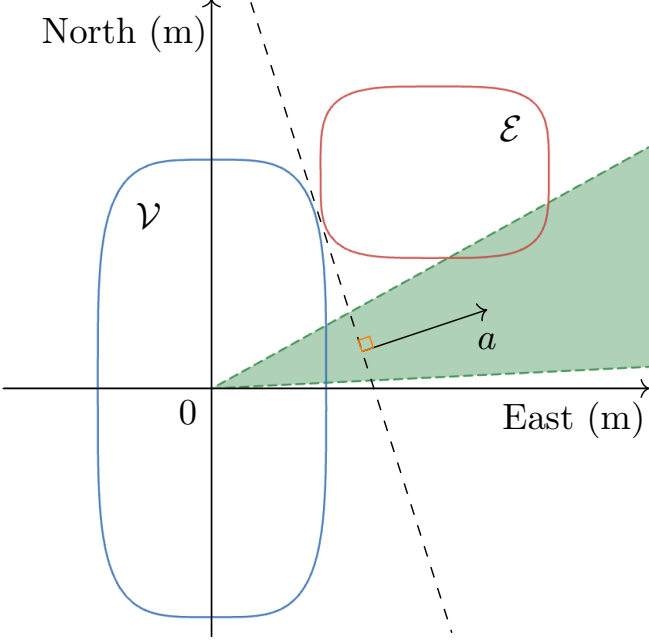


Fig. 2. Disjoint sets \mathcal{V} and \mathcal{E} , lying in opposite open halfspaces on either side of a dashed black hyperplane. The corresponding separating axis is labeled a . The green set — which does not include the origin — is all the separating axes that satisfy the condition in Equation (4) for this scenario.

$\sup_{x \in \mathcal{V}} \langle a, x \rangle \geq \langle a, y \rangle \geq \inf_{x \in \mathcal{E}} \langle a, x \rangle$, which contradicts Equation (4). \square

In this paper, an axis a that satisfies (4) is called a separating axis. Fig. 2 illustrates an example of a separating axis; The condition can be equivalently written as

$$\delta_{\mathcal{V}}^*(a) + \delta_{-\mathcal{E}}^*(a) < 0. \quad (5)$$

Lastly, note that for safety reasons, the vehicle superellipsoid is enlarged, therefore, the strict inequality in (5) can be replaced by \leq .

3.3 Collision avoidance condition

The vehicle and obstacles are modeled by closed superellipsoids. Let us define the vehicle $\mathcal{V} = \{R_{\theta}^v S^v x + c^v \mid x \in \mathcal{B}_p\}$, and an obstacle as $\mathcal{E} = \{R_{\theta}^e S^e x + c^e \mid x \in \mathcal{B}_p\}$. The support function of \mathcal{V} at a is

$$\begin{aligned} \delta_{\mathcal{V}}^*(a) &= \sup_{w \in R_{\theta}^v S^v \mathcal{B}_p + c^v} \langle a, w \rangle \\ &= \sup_{d \in R_{\theta}^v S^v \mathcal{B}_p} \langle a, d + c^v \rangle \text{ where } d = w - c^v \\ &= \delta_{R_{\theta}^v S^v \mathcal{B}_p}^*(a) + \langle a, c^v \rangle. \end{aligned} \quad (6)$$

Similarly, as the sets $R_{\theta} S \mathcal{B}_p$ and $-R_{\theta} S \mathcal{B}_p$ are equal, the support function of $-\mathcal{E}$ at a is

$$\delta_{-\mathcal{E}}^*(a) = \delta_{R_{\theta}^e S^e \mathcal{B}_p}^*(a) + \langle a, -c^e \rangle. \quad (7)$$

The support function of a superellipsoid centered at the origin is the dual of the p -norm (Bauschke and Combettes, 2017, Sec. 7.2) $\delta_{R_{\theta} S \mathcal{B}_p}^*(a) = \|S R_{\theta}^T a\|_q$, where $p \in [2, \infty)$, and p and q are conjugate exponents, i.e., $\frac{1}{p} + \frac{1}{q} = 1$. The pair $(p, q) = (1, \infty)$ is valid and $\|x\|_{\infty} = \max_i |x_i|$. Now, we can express Equation (5) as

$$\|S^v R_{\theta}^{vT} a\|_q + \|S^e R_{\theta}^{eT} a\|_q + \langle a, c^v - c^e \rangle < 0. \quad (8)$$

The set of all a that satisfy the condition in Equation (8) is closed under positive scalar multiplication, therefore, we can assume that $\|a\|_2 = 1$.

4. HIERARCHICAL NMPC DESIGN

A two-layer hierarchical NMPC is implemented to control the vehicle. The high-level trajectory-planning controller is denoted HC and the low-level trajectory-following controller is denoted LC. The input to HC includes the vehicle state, the target state, and any obstacles. The output is a list of the vehicle's state at each predicted stage. The input to LC includes the trajectory output of HC, which LC is assumed to follow closely. The output of LC is the throttle and spin inputs for the vehicle to follow the trajectory. In line with the receding horizon control strategy, the first control action from LC is applied to the vehicle's inputs.

To formulate the NMPC problems, we discretize Equations (1) by forward Euler discretization, $f(z_t, u_t) = z_t + T\dot{z}_t$, with sampling time $T > 0$. Then, we define $F_0(z, u) = z$ and recursively $F_{i+1}(z, u) = f(F_i(z, u), u)$. Next, we present the hierarchical NMPC, where the sampling time of LC is $t_L = T$ and HC is τ times slower, $t_H = \tau T$, to allow enough time for the high-level optimization problem to be solved.

4.1 High-level problem

We formulate the high-level problem with the vehicle state $z_t = (c_t, \theta_t, v_t)$ and vehicle input $u_t = (r_t, s_t)$ at stage t , as defined in Section 2, and the system dynamics F_{τ} . The high-level discrete-time trajectory-planning optimal control problem is

$$\mathbb{P}_H : \underset{(u_t)_{t=0}^{H-1}, (z_t)_{t=0}^H, (a_t)_{t=0}^H}{\text{Minimize}} \sum_{t=0}^{H-1} \ell_t(z_t, u_t) + V_f(z_H), \quad (9a)$$

$$\text{s.t. } z_{t+1} = F_{\tau}(z_t, u_t), \quad t \in \mathbb{N}_{[0, H-1]}, \quad (9b)$$

$$|r_t| \leq r_{\max}, \quad t \in \mathbb{N}_{[0, H-1]}, \quad (9c)$$

$$|s_t| \leq s_{\max}, \quad t \in \mathbb{N}_{[0, H-1]}, \quad (9d)$$

$$\begin{aligned} &\|(S^v R_{\theta}^{vT})_t a_t\|_q + \|(S^e R_{\theta}^{eT})_t a_t\|_q \\ &\quad + \langle a_t, c_t^v - c_t^e \rangle \leq 0, \quad t \in \mathbb{N}_{[0, H]}, \end{aligned} \quad (9e)$$

$$\|a_t\|_2 = 1, \quad t \in \mathbb{N}_{[0, H]}, \quad (9f)$$

$$z_0 = z, \quad (9g)$$

for some $p \geq 2$, and $1 \leq \tau \in \mathbb{N}$, where $q = \frac{p}{p-1}$, ℓ_t is the stage cost function at stage t , V_f is the terminal cost function, and $H \in \mathbb{N}$ is the horizon.

To reduce the problem size, $\ell_t(z_t, u_t) = 0$ for all odd t , and for all even t the stage cost function is

$$\begin{aligned} \ell_t(z_t, u_t) &= q_c \|c_t - c_{\text{ref}}\|_2^2 + q_{\theta} (\theta_t - \theta_{\text{ref}})^2 \\ &\quad + q_r r_t^2 + q_{r_{\Delta}} (r_t - r_{t-1})^2 + q_s s_t^2 + q_{s_{\Delta}} (s_t - s_{t-1})^2, \end{aligned}$$

and the terminal cost function is

$$V_f(z_H) = q_{c_H} \|c_H - c_{\text{ref}}\|_2^2 + q_{\theta_H} (\theta_H - \theta_{\text{ref}})^2,$$

where $q_c, q_{\theta}, q_r, q_{r_{\Delta}}, q_s, q_{s_{\Delta}}, q_{c_H}, q_{\theta_H} > 0$ are the weights, c_{ref} is the reference position and θ_{ref} is the reference heading. The weight of q_c and q_{c_H} penalize the Euclidean distance between the vehicle and the target, q_{θ} and q_{θ_H}

penalize the heading difference between the vehicle and the target, q_r and q_s penalize the use of control inputs, and q_{r_Δ} and q_{s_Δ} penalize changes in the control inputs.

4.2 Low-level problem

The solution $(z_t^*)_{t=0}^H$ of \mathbb{P}_H , where $z_t^* = (c_t^*, \theta_t^*, v_t^*)$, is a trajectory towards the target state, comprising states every t_H seconds for LC to follow. The trajectory is tracked by an NMPC that penalizes the difference between the predicted state at stage k and the next state in the planned trajectory after k , at stage $t_k = \max\{1, \lceil \tau^{-1}k \rceil\}$, where $\lceil \cdot \rceil$ is the ceiling function.

The trajectory tracking is similar to the two and a half carrots method of Reiter and Abel (2015), where the most important predicted state is at the beginning rather than the end. In LC, the stage of the most important state is denoted ω and is selected so that ω is a multiple of τ , is close to the beginning of the planned trajectory, and the trajectory is updated before the vehicle has time to reach it, e.g., $\omega = 2\tau$. This results in good trajectory-following performance as the vehicle prioritizes following the trajectory immediately before it, rather than the vehicle's state at the end of the trajectory.

We differentiate notation that appear in both problems by an overline on the low-level variables and functions. We formulate the low-level problem with the vehicle state $\bar{z}_k = (\bar{c}_k, \bar{\theta}_k, \bar{v}_k)$ and vehicle input $\bar{u}_k = (\bar{r}_k, \bar{u}_k)$ at stage k , as defined in Section 2, and the system dynamics f . The low-level discrete-time trajectory-following optimal control problem is

$$\mathbb{P}_L : \underset{\substack{(\bar{u}_k)_{k=0}^{L-1}, \\ (\bar{z}_k)_{k=0}^L}}{\text{Minimize}} \sum_{k=0}^{L-1} \bar{\ell}(\bar{z}_k, \bar{u}_k) + V_\omega(\bar{z}_\omega, \bar{u}_\omega) + \bar{V}_f(\bar{z}_L), \quad (10a)$$

$$\text{s.t. } \bar{z}_{k+1} = f(\bar{z}_k, \bar{u}_k), \quad k \in \mathbb{N}_{[0, L-1]}, \quad (10b)$$

$$|\bar{r}_k| \leq r_{\max}, \quad k \in \mathbb{N}_{[0, L-1]}, \quad (10c)$$

$$|\bar{s}_k| \leq s_{\max}, \quad k \in \mathbb{N}_{[0, L-1]}, \quad (10d)$$

$$\bar{z}_0 = \bar{z}, \quad (10e)$$

for some $\omega \in \mathbb{N}_{[0, L-1]}$, where $\bar{\ell}$ is the stage cost function, V_ω is a high-weighted stage cost function, \bar{V}_f is the terminal cost function, and $L \in \mathbb{N}$ is the horizon. The horizon time of \mathbb{P}_H must be longer than that of \mathbb{P}_L in order for the planned trajectory to have enough states to follow, i.e., $Lt_L < Ht_H$.

The stage cost function is

$$\bar{\ell}(\bar{z}_k, \bar{u}_k) = \bar{q}_c \|\bar{c}_k - c_{t_k}^*\|_2^2 + \bar{q}_\theta (\bar{\theta}_k - \theta_{t_k}^*)^2 + \bar{q}_r \bar{r}_k^2 + \bar{q}_{r_\Delta} (\bar{r}_k - \bar{r}_{k-1})^2 + \bar{q}_s \bar{s}_k^2 + \bar{q}_{s_\Delta} (\bar{s}_k - \bar{s}_{k-1})^2,$$

the high-weighted stage cost function is

$$V_\omega(\bar{z}_\omega, \bar{u}_\omega) = \bar{q}_{c_\omega} \|\bar{c}_\omega - c_{t_k}^*\|_2^2 + \bar{q}_{\theta_\omega} (\bar{\theta}_\omega - \theta_{t_k}^*)^2 + \bar{q}_r \bar{r}_k^2 + \bar{q}_{r_\Delta} (\bar{r}_k - \bar{r}_{k-1})^2 + \bar{q}_s \bar{s}_k^2 + \bar{q}_{s_\Delta} (\bar{s}_k - \bar{s}_{k-1})^2,$$

and the terminal cost function is

$$\bar{V}_f(\bar{z}_L) = \bar{q}_{c_L} \|\bar{c}_\omega - c_{t_k}^*\|_2^2 + \bar{q}_{\theta_L} (\bar{\theta}_\omega - \theta_{t_k}^*)^2, \quad (11)$$

where $\bar{q}_c, \bar{q}_\theta, \bar{q}_r, \bar{q}_{r_\Delta}, \bar{q}_s, \bar{q}_{s_\Delta}, \bar{q}_{c_\omega}, \bar{q}_{\theta_\omega}, \bar{q}_{c_L}, \bar{q}_{\theta_L} > 0$ are the weights. The weight of $\bar{q}_c, \bar{q}_{c_\omega}$ and \bar{q}_{c_L} penalize the Euclidean distance between the vehicle and the target, $\bar{q}_\theta, \bar{q}_{\theta_\omega}$

and \bar{q}_{θ_L} penalize the heading difference, \bar{q}_r and \bar{q}_s penalize the use of control inputs, and \bar{q}_{r_Δ} and \bar{q}_{s_Δ} penalize changes in the control inputs.

4.3 Tuning

To avoid local minima when solving \mathbb{P}_H , we have two solvers: one solver is enabled constantly and we warm-start this solver's separating axes with the vectors from the vehicle's current center to the corresponding obstacle's center, that is, $((c_i^e - c_0^v)_i)_t, i \in \mathbb{N}_{[1, M]}, t \in \mathbb{N}_{[0, H]}$, where c_0^v is the vehicle's center at stage $t = 0$. This is inspired by the approach in (Ericson, 2004, Sec. 5.2.1) for polyhedral objects. The other solver is enabled when a previous solution that converged is available. When both solvers are enabled, they run in parallel and the output solution of the solver that converges with the lowest cost is used. Then, the solution trajectory is accepted if it has an adequately low measure of infeasibility¹, which is provided by the OpEn solver. If not, the vehicle continues on the last accepted trajectory.

Simulation. We use basic model parameters for simulations; they are $\alpha = 1.0, \beta = 0.2, v_{\max} = 1.0$. Both HC and LC restrict the control inputs to $r_{\max} = 1.0$ and $s_{\max} = 1.0$. The HC solves \mathbb{P}_H with $q_c = 1, q_\theta = 0, q_r = 0.01, q_s = 0.5, q_{r_\Delta} = 0, q_{s_\Delta} = 0, q_{c_H} = 20, q_{\theta_H} = 0, t_H = 1s$, and $H = 40$, looking 40s into the future. The LC solves \mathbb{P}_L with $\bar{q}_c = 100, \bar{q}_\theta = 0, \bar{q}_r = 0.01, \bar{q}_s = 0.1, \bar{q}_{r_\Delta} = 0, \bar{q}_{s_\Delta} = 0, \bar{q}_{c_\omega} = 1000, \bar{q}_{\theta_\omega} = 0, \bar{q}_{c_L} = 100, \bar{q}_{\theta_L} = 0, t_L = 0.1s$ so $T = 0.1, \tau = 10$, and $\omega = 20$, and $L = 100$, looking 10s into the future.

Demonstration. We use experimental data to estimate the model parameters in Section 2; they are $\alpha = 0.4, \beta = 0.15, v_{\max} = 1.0$. Both HC and LC restrict the control inputs to $r_{\max} = 0.5$ and $s_{\max} = 0.2$. The HC solves \mathbb{P}_H with $q_c = 100, q_\theta = 0, q_r = 0.01, q_s = 7, q_{r_\Delta} = 0, q_{s_\Delta} = 0.01, q_{c_H} = 5000, q_{\theta_H} = 0, t_H = 1s$, and $H = 40$, looking 40s into the future. Moreover, LC solves \mathbb{P}_L with $\bar{q}_c = 100, \bar{q}_\theta = 0, \bar{q}_r = 0.1, \bar{q}_s = 0.1, \bar{q}_{r_\Delta} = 5, \bar{q}_{s_\Delta} = 5, \bar{q}_{c_\omega} = 1000, \bar{q}_{\theta_\omega} = 0, \bar{q}_{c_L} = 100, \bar{q}_{\theta_L} = 0, t_L = 0.1s$ so $T = 0.1, \tau = 10$, and $\omega = 20$, and $L = 100$, looking 10s into the future.

4.4 Embedded numerical optimization

OpEn solves parametric nonconvex problems of the form

$$\mathbb{P}(\xi) : \underset{\mathbf{u} \in \mathbb{R}^n}{\text{Minimize}} \quad g(\xi, \mathbf{u}), \quad (12a)$$

$$\text{s.t. } \mathbf{u} \in \mathcal{U}, \quad (12b)$$

$$G_1(\xi, \mathbf{u}) \in \mathcal{C}, \quad (12c)$$

$$G_2(\xi, \mathbf{u}) = 0, \quad (12d)$$

where \mathbf{u} is the decision variable and ξ is a parameter vector. Briefly, the requirements are that g is a smooth function with Lipschitz gradient, G_1 and G_2 satisfy certain regularity conditions, \mathcal{U} is closed and can be projected onto, and the set \mathcal{C} is closed, convex, and the point-to-set distance can be computed (Sopasakis et al., 2020).

¹ That is, if the infinity-norm of successive estimates of the Lagrange multipliers is less than a tolerance (0.001) times the current penalty. This is a measure of the distance between $G_1(\xi, \mathbf{u})$ and \mathcal{C} , i.e., a measure of infeasibility of Equation (12c).

Within the algorithm of OpEn, constraints of the type (12b) are imposed by projecting onto \mathcal{U} , (12c) by using the augmented Lagrangian method (ALM), and (12d) by using the quadratic penalty method (PM).

In particular, to solve \mathbb{P}_H we first eliminate the sequence of states using the single shooting approach (Sopasakis et al., 2020), that carries out the minimization over the sequence of control actions. Then, we use (12b) to cast Constraints (9c), (9d), and (9f), and (12c) for (9e). Note that while (9e) can be cast in the form of both (12c) and (12d), the ALM significantly outperforms the PM in this case.

Regarding \mathbb{P}_L , we use the single shooting formulation again and (10c) and (10d) are projectable constraints of the form (12b).

Remark: High values of p can lead to poorly conditioned problems. To mitigate this, one can start by solving \mathbb{P}_H where $p_0 = 2$, increase the value of p via $p_{i+1} = \min(p_{\text{target}}, \gamma p_i)$ for some $p_{\text{target}} \geq 2$ and $\gamma > 1$, and warm-start \mathbb{P}_H where $p = p_{i+1}$ with the solution of \mathbb{P}_H where $p = p_i$. This continuation trick can decrease the runtime.

5. MINIMUM VOLUME BOUNDING SUPERELLIPSOIDS

The LiDAR sensor updates a 0.6m^2 grid around the vehicle. Each grid cell is either an obstacle, or not. Instead of treating each obstacle cell independently and increasing the computation cost of the solver, a cluster of these cells can be bounded by one superellipsoid. Clustering is a common problem with readily available solutions. One of the most widely used algorithms is k -means clustering (Hartigan and Wong, 1979). Note that fitting superellipsoids to clusters has been explored (Rosin, 2000).

We extend (Sun and Freund, 2004) to model objects with minimum volume bounding superellipsoids (MVBS) rather than ellipsoids, through a grid search and optimization-based method. Equation (2), can be rearranged to

$$\mathcal{X} = \{x \in \mathbb{R}^2 : \|(R_\theta S)^{-1}(x - c)\|_p \leq 1\}, \quad (13)$$

and the area A inside \mathcal{X} can be expressed by (Rosin, 2000)

$$A = s_1 s_2 \frac{4\Gamma(1 + 1/p)^2}{\Gamma(1 + 2/p)}, \quad (14)$$

where Γ is the gamma function (Farrell and Ross, 2013, Sec. 1). Therefore, A is proportional to $s_1 s_2$ for a constant p , and A is rotation invariant. Now, computing the MVBS boils down to solving the bilinear problem

$$\underset{s_1, s_2 > 0}{\text{Minimize}} \quad s_1 s_2, \quad (15a)$$

$$\text{subject to} \quad \|S^{-1}R_\theta^T(m_i - c)\|_p \leq 1, \quad i \in \mathbb{N}_{[1, 4M]}, \quad (15b)$$

where M is the number of obstacle cells and m_i is each obstacle cell vertex. To solve the problem in Equations (15), we first compute the average of the unique obstacle cell vertices, and use this to find a bounding rectangle using a grid search on $\theta \in [0, \pi/2)$ in 17 steps. Then, an OpEn solver is warm-started with the center, scaling, and θ of the rectangle and the MVBS solution is shown in Fig. 3. The bounding constraint in Equation (15b) is imposed by the penalty method. On an NVIDIA Jetson TX2 fitted for *Moe*, over 10000 runs, the 95th percentile of the computation time for the grid search was 13.67 ms and for the

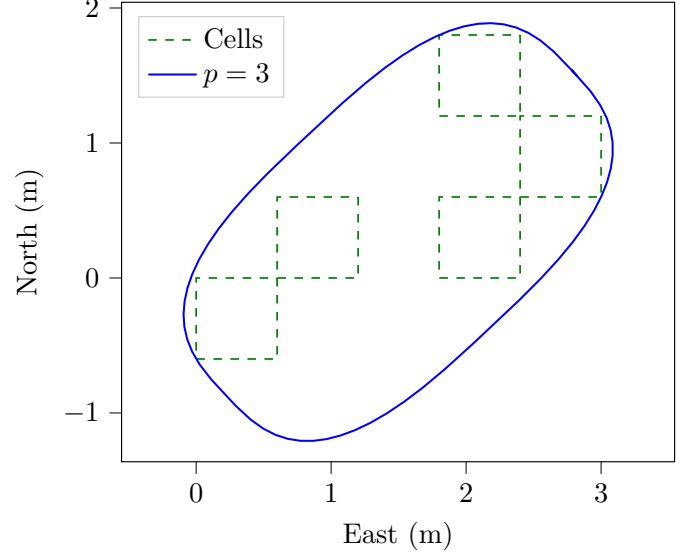


Fig. 3. Minimum volume bounding superellipsoid that illustrates how complex obstacles can be modeled by a simple object. The dashed green squares are a cluster of obstacle grid cells.

solver with $p = 3$ was 3.55 ms, with $p = 2$ was 2.38 ms, and with $p = 4$ was 3.49 ms.

6. SIMULATION

We present two simulations that were run on an NVIDIA Jetson TX2 fitted for *Moe*. For both simulations, the initial vehicle position was $(13, -6)$ and the target point was $(-13, 6)$ (see Fig 4). The obstacles are superellipsoids with parameters $c_1 = 0, c_2 = -10, s_1 = 5, s_2 = 9.5, \theta = 0$ rad for the West obstacle, and $c_1 = 0, c_2 = 10, s_1 = 5, s_2 = 8, \theta = 0$ rad, for the East one. The vehicle was modeled by a superellipsoid with parameters $s_1 = 2.0$ and $s_2 = 1.1$. All objects were modeled with $p = 3$.

Fig. 4 illustrates two simulations with initial headings $\theta = 90^\circ$ for trajectory A and $\theta = -170^\circ$ for trajectory B. Fig. 5 illustrates the runtimes of the high- and low-level solvers during both simulations. The low-level controller has a median execution time of 1.3 ms (max 15 ms), and the high-level controller has a median of 183 ms (max 676 ms).

7. DEMONSTRATION

A demonstration of the hierarchical controller on one of EquipmentShare’s CTLs was run at their R&D facility. The vehicle autonomously navigates around an obstacle to the target. The demonstration is available online at <https://youtu.be/HLNVZtbsl0c>. The logged vehicle states are plotted in Fig. 6 and the logged vehicle control inputs are plotted in Fig. 7. Fig. 8 demonstrates how LC closely follows the trajectory planned by HC while the trajectory is updated.

The initial vehicle position was $(-103.68, 77.51)$ and the target position was $(-79.50, 61.40)$. The virtual obstacle was modeled by a superellipsoid with parameters $c_1 = -92.2, c_2 = 69.8, s_1 = 1.0, s_2 = 1.5$, and $\theta = -0.5$ rad. The

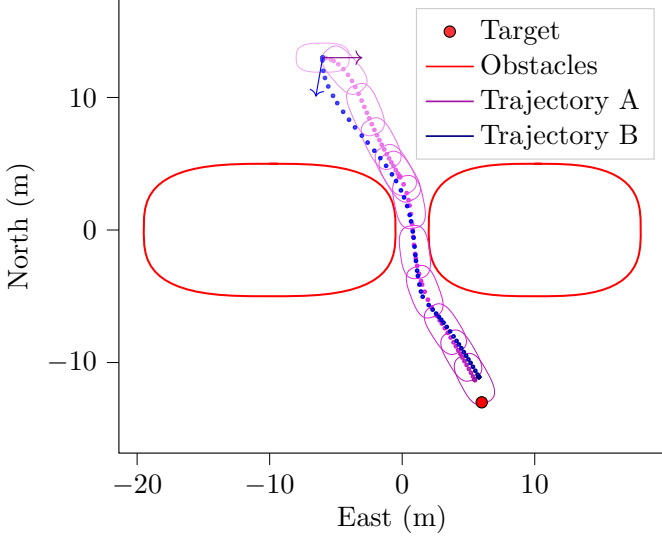


Fig. 4. Two simulated trajectories of a vehicle with Python. The red superellipsoids are obstacles. The green circle is the target. The trajectories have the same start and target position. One vehicle starts with heading $\theta = 90^\circ$ and the other with $\theta = -170^\circ$.

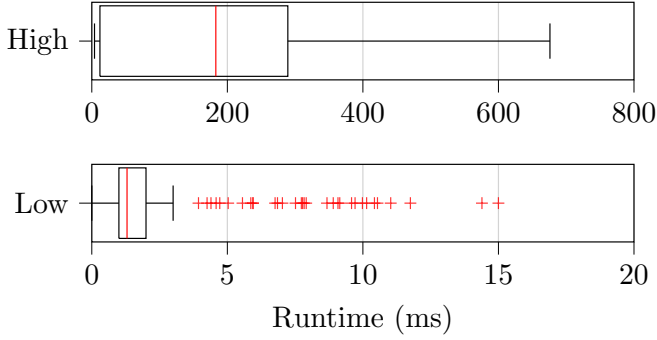


Fig. 5. High- and low- level solver runtime data collected during both simulations (cf Fig. 4).

vehicle was modeled by a superellipsoid with parameters $s_1 = 2.0$ and $s_2 = 1.1$. Both were modeled with $p = 3$.

During the demonstration, the solver in HC that converged with the lowest cost had a 95th percentile runtime of 185.68 ms with a maximum of 900 ms, and the solver in LC had a 95th percentile runtime of 6.36 ms with a maximum of 90 ms. The maximum runtimes are 90% of the solver's sampling time. As a safety measure, if LC reaches its maximum runtime, the control input is set to zero so the vehicle does not move. If HC reaches its maximum runtime, LC continues to track the last HC trajectory. Neither solver reached its maximum runtime during the demonstration.

8. CONCLUSIONS AND FUTURE WORK

We developed a novel approach to obstacle avoidance in NMPC, leveraging a combination of the separating hyperplane theorem and superellipsoids. We proposed a tractable collision avoidance condition, showed how complex obstacles can be bounded by superellipsoids, and

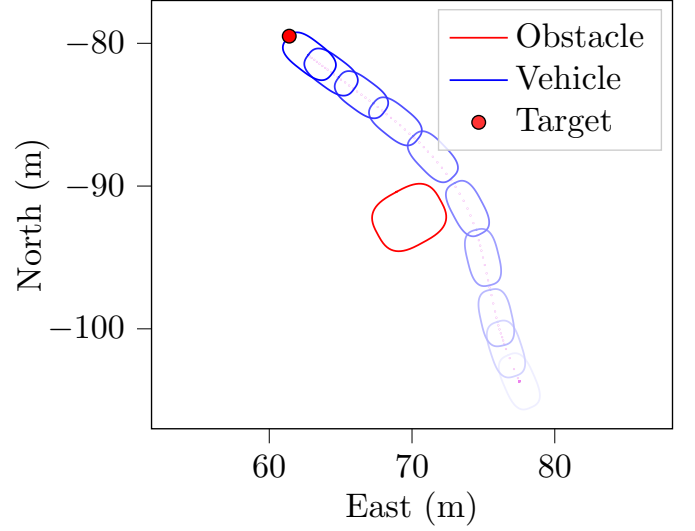


Fig. 6. Vehicle state data collected during demonstration. The demonstration ends when the vehicle reaches within a meter of the target position. The blue superellipsoids depict the vehicle, growing darker as time evolves.

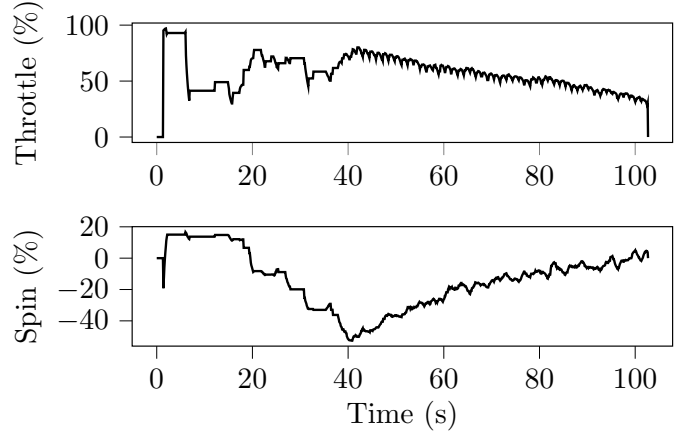


Fig. 7. Throttle and spin control actions from LC during the demonstration. The vehicle initially considers turning left to go around the obstacle, then decides on a trajectory to the right of the obstacle.

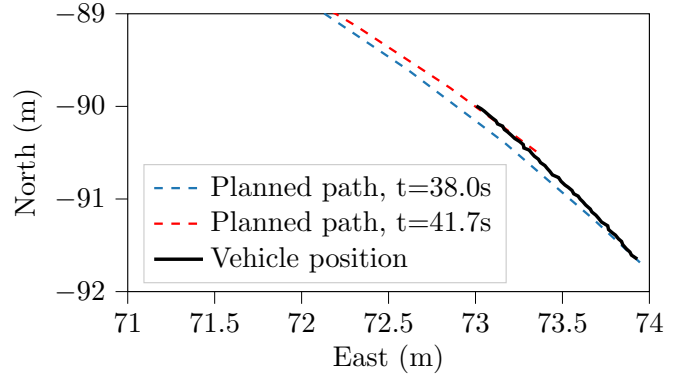


Fig. 8. Close-up view of Fig. 6 demonstrating the vehicle position closely following the planned trajectory while the trajectory is updated.

demonstrated the efficacy and real-time capability of the approach through simulations and experimental results.

The use of superellipsoids for object representation has shown to be advantageous in comparison to modeling with ellipsoids, as rectangular geometries that are often encountered in real-world scenarios — such as vehicles and buildings — can be more accurately described with the same complexity.

REFERENCES

- Bauschke, H.H. and Combettes, P.L. (2017). *Convex Analysis and Monotone Operator Theory in Hilbert Spaces*. Springer.
- Boyd, S.P. and Vandenberghe, L. (2004). *Convex optimization*. Cambridge University Press.
- Cai, G., Chen, B.M., and Lee, T.H. (2011). *Unmanned rotorcraft systems*. Springer Science & Business Media.
- Crane III, C.D., Armstrong II, D.G., and Rankin, A.L. (1995). Autonomous navigation of heavy construction equipment. *Comp-Aided Civ Infr Eng*, 10(5), 357–370.
- Ericson, C. (2004). *Real-time collision detection*. CRC Press.
- Farrell, O.J. and Ross, B. (2013). *Solved problems in analysis: As applied to gamma, beta, legendre and bessell functions*. Courier Corporation.
- Gai, S.N., Sun, R., Chen, S.J., and Ji, S. (2019). 6-DOF robotic obstacle avoidance path planning based on artificial potential field method. In *UR*, 165–168. IEEE.
- Gridgeman, N.T. (1970). Lamé ovals. *The Mathematical Gazette*, 54(387), 31–37.
- Grüne, L., Pannek, J., Grüne, L., and Pannek, J. (2017). *Nonlinear model predictive control*. Springer.
- Hartigan, J.A. and Wong, M.A. (1979). Algorithm AS 136: A k-means clustering algorithm. *Journal of the Royal Statistical Society. Series C (Applied statistics)*, 28(1), 100–108.
- Khan, R., Malik, F.M., Raza, A., and Mazhar, N. (2021). Comprehensive study of skid-steer wheeled mobile robots: Development and challenges. *Int J Rob Res Appl*, 48(1), 142–156.
- Khan, S. (2022). *Design, testing and validation of model predictive control for an unmanned ground vehicle*. Ph.D. thesis, UNSW Sydney.
- LaValle, S.M. (2006). *Planning algorithms*. Cambridge University Press.
- Liu, J., Jayakumar, P., Stein, J.L., and Ersal, T. (2018). A nonlinear model predictive control formulation for obstacle avoidance in high-speed autonomous ground vehicles in unstructured environments. *Vehicle system dynamics*, 56(6), 853–882.
- Melenbrink, N., Werfel, J., and Menges, A. (2020). On-site autonomous construction robots: Towards unsupervised building. *Automation in construction*, 119, 103312.
- Menon, M.S., Ravi, V., and Ghosal, A. (2017). Trajectory planning and obstacle avoidance for hyper-redundant serial robots. *J Mechan Robot*, 9(4), 041010.
- Patle, B., Pandey, A., Parhi, D., Jagadeesh, A., et al. (2019). A review: On path planning strategies for navigation of mobile robot. *Defence Technology*, 15(4), 582–606.
- Pauls, J.H., Boxheimer, M., and Stiller, C. (2022). Real-time cooperative motion planning using efficient model predictive contouring control. In *IV Symposium*, 1495–1503. IEEE.
- Rafai, A.N.A., Adzhar, N., Jaini, N.I., et al. (2022). A review on path planning and obstacle avoidance algorithms for autonomous mobile robots. *J Robot*, 2022.
- Reiter, M. and Abel, D. (2015). Two and a half carrots – a versatile and intuitive optimisation-based path-following approach for road vehicles. In *MED*, 364–370. IEEE.
- Rosin, P.L. (2000). Fitting superellipses. *IEEE Transactions on Pattern Analysis and Machine Intelligence*, 22(7), 726–732.
- Sathya, A., Sopasakis, P., Van Parys, R., Themelis, A., Pipeleers, G., and Patrinos, P. (2018). Embedded nonlinear model predictive control for obstacle avoidance using PANOC. In *ECC*, 1523–1528.
- Scattolini, R. (2009). Architectures for distributed and hierarchical model predictive control – a review. *J Proc Contr*, 19(5), 723–731.
- Smith, N.E., Arendt, C.D., Cobb, R.G., and Reeger, J.A. (2017). Implementing conditional inequality constraints for optimal collision avoidance. *J Aeron Aersp Eng*.
- Sopasakis, P., Fresk, E., and Patrinos, P. (2020). OpEn: Code generation for embedded nonconvex optimization. In *IFAC World Congress*. Berlin.
- Sun, P. and Freund, R.M. (2004). Computation of minimum-volume covering ellipsoids. *Operations Research*, 52(5), 690–706.
- Teizer, J., Allread, B.S., Fullerton, C.E., and Hinze, J. (2010). Autonomous pro-active real-time construction worker and equipment operator proximity safety alert system. *Automation in construction*, 19(5), 630–640.
- Weisstein, E.W. (2002). *CRC concise encyclopedia of mathematics*. CRC Press.
- Xue, Z. and Gonsalves, T. (2021). Vision based drone obstacle avoidance by deep reinforcement learning. *AI*, 2(3), 366–380.